On the predictability of springtime ozone depletion events using the ECCC Global Deterministic Prediction System

Jean de Grandpré [1], Irena Ivanova [1], Yves J. Rochon [2], Caroline Jouan [3]
and Paul A. Vaillancourt [4]

[1] *Air Quality Research Division, Environment and Climate Change Canada, Dorval, Canada*

[2] *Air Quality Research Division, Environment and Climate Change Canada, Downsview, Canada*

[3] *Canadian Meteorological Center, Environment and Climate Change Canada, Dorval, Canada*

[4] *Meteorological Research Division, Environment and Climate Change Canada, Dorval, Canada*

Corresponding author: Jean de Grandpré, jean.degrandpre@ec.gc.ca

Author Three now at the CICERO Center for International Climate Research, Oslo, Norway

ABSTRACT: Ozone depletion events are recurring phenomena in both polar regions, characterized by significant interannual variability. In this study, the Environment and Climate Change Canada (ECCC) Global Deterministic Prediction System is used to investigate the medium-range predictability of ozone and weather throughout the anomalous polar ozone depletion events of 2020. The system includes ozone assimilation and makes use of a prognostic ozone field for the computation of heating rates. The ozone scheme uses simplified photochemical modules to represent the impact of both gas-phase and heterogeneous reactions throughout polar ozone depletion events. The study shows that during the Boreal and Austral spring seasons, the predictability of the total ozone column exceeds 10 days and is comparable to the predictability of large-scale weather variables. It also demonstrates that over both polar regions, the inclusion of ozone radiative coupling has a significant impact on the temperature and wind distributions throughout the stratosphere. Over Antarctica, the ozone coupled forecasts are systematically colder at all lead times, which helps eliminate a temperature bias present in the model using climatological ozone. The strength of the polar vortex also increases significantly throughout the lower stratosphere, in better agreement with zonal wind analyses. Over the Arctic the use of an ozone-interactive model also produces significant changes in the temperature and wind forecasts, but the impact on the quality of the weather forecasts is generally neutral. The study shows the overall benefits of using ozone coupled models in the highly perturbed springtime conditions of the polar regions.

SIGNIFICANCE STATEMENT: Ozone hole events which occur during springtime over polar regions can be predicted several days ahead using Numerical Weather Prediction (NWP) systems. The ozone decrease associated with such events reduces the absorption of solar radiation, impacting the temperature and wind fields in the lower stratosphere at an altitude of about 15-20 km. This study shows that including this process within an NWP model can improve weather forecasts in the lower stratosphere. The impact of this process has been evaluated during the severe springtime ozone depletion events that took place in both polar regions in 2020. The study demonstrates that over Antarctica, using an ozone coupled model produces a stronger and colder stratospheric polar vortex in better agreement with temperature and wind analyses. Overall, the study highlights the benefits of using ozone coupled models in the highly perturbed springtime conditions of the polar regions.

1. Introduction

Even though the ozone layer is slowly recovering after several decades of decline (WMO 2018), it remains fragile to extreme meteorological conditions. Indeed, the 2020 springtime ozone depletion events in both hemispheres have been among the strongest on record in terms of depth, size, and duration (Lawrence et al. 2020; Manney et al. 2020; Inness et al. 2020). Forecasting such events is important for populations living at high latitudes, who are potentially exposed to harmful UV radiation (Hand 2016; Witze 2020). Strengthening our forecasting capabilities to address such issues will also contribute to improving our comprehension of these phenomena.

The formation of ozone holes is driven by catalytic reactions involving short-lived halogen compounds. The presence of these species within the stratospheric polar regions is due to the photodissociation of chlorofluorocarbons and halons released from anthropogenic activities. The conversion of these long-lived constituents into chemically active species takes place through heterogeneous reactions occurring on the surface of Polar Stratospheric Clouds (PSC) (Solomon 1999). The ozone loss associated with these processes can be resolved using different types of models with various levels of complexity (Geer et al. 2006, 2007). In the context of NWP applications, they can be represented with simplified approaches as a way to minimize the usage of computing resources (Eskes et al. 2002; Sekiyama and Shibata 2005; Stajner et al. 2006; Flemming et al. 2011; Monge-Sanz et al. 2011).

3

The predictability of ozone varies significantly during the various stages of ozone depletion events (Flemming et al. 2011). The quality of ozone forecasts at synoptic timescales depends primarily on the availability of comprehensive analyses that serve as initial conditions. During the deepening of the ozone hole, it also depends on the representation of photochemical processes, whereas the representation of ozone transport is particularly important during the ozone recovery period. The predictability of ozone throughout these events also relies on the quality of weather forecasts, which determine the temperature and wind distributions.

Ozone forecasting systems are generally based on comprehensive NWP models that include a lid well above the stratopause and incorporate different parameterization schemes for representing radiative and gravity wave drag processes. These components are necessary for resolving the Brewer-Dobson Circulation, which determines the seasonal and interannual variability of the middle atmosphere (Scaife et al. 2022). The use of high-top models is valuable for improving the representation of other phenomena such as Sudden Stratospheric Warmings (Baldwin et al. 2021), Arctic Oscillations, and Quasi-Biennial Oscillations (Scaife et al. 2014; Wang et al. 2022), which also contribute to increasing the weather and ozone predictability in the stratosphere and below through downward control (Haynes et al. 1991; Baldwin and Dunkerton 1999).

The use of ozone as a prognostic constituent in NWP systems allows us to resolve the complex dynamical, radiative, and photochemical interactions that take place during ozone hole phenomena (Haase and Matthes 2019; Ménard et al. 2019; Monge-Sanz et al. 2022; de Grandpré et al. 2009). The radiative response is directly associated with the decrease in solar heating resulting from the rapid disappearance of ozone within the polar vortex. The associated cooling contributes to the enhancement of the ozone depletion process, which enhances the Polar Night Jet (PNJ) through thermal wind balance. This mechanism decreases the mixing of low ozone within the polar vortex with ozone-rich air from the lower latitudes, which in turn contributes to further cooling of the polar vortex. This positive feedback mainly occurs under the conditions of a strong PNJ, often prevailing during Southern Hemisphere springtime periods. Climate studies have shown that resolving the non-zonal component of the radiative forcing generally reduces ozone heating and produces a significant delay in the final breakup of the vortex (Crook et al. 2008; Gillet et al. 2009).

The strengthening of the polar vortex can also generate a dynamical response through its impact on the propagation of planetary waves in the middle atmosphere (Andrews et al. 1987; Charney

and Drazin 1961). The nature of the response will depend on the strength of the PNJ, varying from year to year in the polar regions. In the Southern Hemisphere, the increase of the PNJ will generally preclude the propagation of large-scale planetary waves, which can strengthen the initial ozone-induced radiative forcing. With the presence of a weak polar vortex, as frequently occurs in the Arctic, the strengthening of the PNJ can enhance wave activity and increase the number of wave-breaking events, contributing to the strengthening of the downwelling branch of the Brewer-Dobson Circulation. The associated adiabatic warming in this case can counteract the original radiative forcing and lead to an early breakup of the polar vortex (Lin et al. 2017). The nature of these interactions depends on the preconditioning of the polar vortex (Lawrence and Manney 2020), which can vary throughout the springtime period.

The quality of ozone and weather forecasts can be evaluated against observations and analyses in different regions at different lead times using standard measures such as Anomaly Correlation Coefficient (ACC) and root mean square errors (Geer 2016). ACC provides a measure of predictability in terms of timescales and can be applied to different fields, including Total Ozone Column (TOC), which serves as an excellent proxy for characterizing the ozone distribution in the lower stratosphere. TOC can be measured accurately from satellites and ground-based instruments, and its predictability is comparable to the predictability of large-scale weather variables such as temperature and geopotential height throughout the lower stratosphere. Being an integrated quantity, TOC needs to be evaluated in combination with other measures such as volume mixing ratio to assess species vertical distribution. TOC is widely used for assessing ozone forecasting systems in the lower stratosphere, where in-situ observations are sparse (Eskes et al. 2002; Sekiyama and Shibata 2005; Stajner et al. 2006).

In this study, the ECCC Global Deterministic Prediction System (GDPS) is used to determine the ozone and weather predictability during the Boreal and Austral ozone hole events of 2020. The impact of including ozone radiative coupling with a simplified heterogeneous chemistry scheme is evaluated during the different stages of these events. The system is run in different configurations to isolate the impact of these different model components on the quality of the weather forecasts. The GDPS is evaluated in both polar regions at the time when ozone depletion was particularly intense. The ozone and weather forecasts of several variables, including temperature and zonal wind, are evaluated against analyses at different lead times. The study includes a description of

the model and the assimilation system in Sections 2 and 3, respectively. The results and analyses are presented in Section 4, and the main conclusions are summarized in Section 5.

2. The ozone coupled NWP model

The ozone coupled GDPS has been in operation at ECCC since November 2021, making it the first global NWP system to incorporate ozone radiative coupling for operational use. This system is based on the Global Environmental Multiscale (GEM) NWP model, which has a dynamical core that solves the fully compressible governing equations using an implicit two-time level Semi-Lagrangian advection scheme (Côté et al. 1998; Girard et al. 2014; Husain and Girard 2017). The current operational system runs at 15 km resolution on 84 levels with a lid at 0.1 hPa (Charron et al. 2012). All model configurations employ the Arakawa-C staggering on a global latitude-longitude grid using the Yin-Yang strategy, represented by a pair of overlapping limited-area grids (Qaddouri and Lee 2011). Vertically, equations are discretized on a terrain-following log-hydrostatic-pressure coordinate (Girard et al. 2014).

In this study, all experiments are conducted with the same model configuration as the one utilized in operation, except for the use of a 25 km horizontal resolution to save computing resources. The physical parameterization packages are from McTaggart-Cowan et al. (2019), which are used by the global and regional operational weather forecasting systems. It includes a non-orographic gravity wave drag parameterization scheme (Hines 1997) that incorporates sources initiated by imbalances and geostrophic adjustments related to convection, fronts, and other transient mesoscale phenomena. Radiative processes are parameterized with the correlated-k distribution approach following Li and Barker (2005), which solves radiative transfer equations in nine longwave and four shortwave spectral bands. For the computation of heating rates, the model uses a prognostic ozone representation based on a simplified photochemical scheme described below.

a. Linearized stratospheric ozone chemistry and equilibrium state

The use of linearized schemes in NWP models allows for the inclusion of a prognostic representation of ozone while minimizing the CPU load on supercomputers (Geer et al. 2007). These approaches use comprehensive models to generate a set of coefficients, which are then used as input to a linearized model. Several linearized schemes are available for including ozone as a

prognostic constituent in NWP systems, such as CD (Cariolle and Teyssèdre 2007), CHEM2D (McCormack et al. 2006), LINOZ (McLinden et al. 2000), and BMS (Monge-Sanz et al. 2011). These schemes vary in complexity and are used to linearize various processes that determine the ozone distribution throughout the model domain. The CD and CHEM2D schemes use 2-D models for linearizing species transport and gas-phase photochemical processes throughout the stratospheric domain. The LINOZ scheme uses a comprehensive box model that only serves for the linearization of gas-phase reactions.

The CD, CHEM2D, and LINOZ schemes do not incorporate heterogeneous reactions into the linearization process. The impact of these reactions needs to be parameterized as an additional process for the study of polar ozone depletion issues. The simplified parameterization schemes used to address such issues generally use prescribed parameters to represent the chemical ozone loss within the polar vortex. They may require some tuning procedures to adjust the ozone loss rates according to a specific timescale within a restricted area. As an alternative, the BMS scheme uses a more comprehensive chemical transport model that includes both gas-phase and heterogeneous reactions for the generation of linear coefficients. Including heterogeneous reactions in the linearization process avoids the need to develop additional photochemical parameterization schemes. The BMS approach can be used for a wide range of applications (Monge-Sanz et al. 2022), making it a valuable alternative in the context of operational NWP forecasting.

At NWP timescales, modeling errors generally increase with time and depend on species' initial conditions. In this study, the length of the forecasts is limited to 10 days, and ozone analyses from the GDPS are used as initial conditions. This experimental framework prevents the development of large forecast errors and makes it possible to use a simplified ozone modeling approach for investigating polar ozone depletion processes. The prognostic ozone scheme used in this study is based on the LINOZ approach, which runs in-line within the GEM NWP model. Following this approach, species transport is resolved explicitly by the model using a Semi-Lagrangian advection scheme (de Grandpré et al. 2016). Ozone tendencies are represented by the first-order Taylor expansion about stratospheric chemical rates and depend on the ozone mixing ratio (ϕ), the temperature (T), and the overhead column ozone c, expressed as follows:

$$\frac{d\phi}{dt} = (P-L)^o + \frac{\partial(P-L)}{\partial\phi}|_o(\phi-\phi^o) + \frac{\partial(P-L)}{\partial T}|_o(T-T^o) + \frac{\partial(P-L)}{\partial c}|_o(c-c^o), \quad (1)$$

where superscripts ^{o} represent climatological values and $|_o$ denotes the evaluation of partial derivatives with respect to the climatological quantities ϕ^o, T^o and c^o. The gas-phase photochemical production and loss terms (P and L) have been computed offline using a comprehensive box model as described in McLinden et al. (2000). All other coefficients have been updated following Hsu and Prather (2009). Below the tropopause, defined as the level where water vapor becomes greater than 10 ppmv, ozone is advected as a passive tracer. Above 1 hPa and below 400 hPa, the ozone mixing ratio is forced toward the model climatology ϕ^o following the expression:

$$\phi(t + \Delta t) = (1 - \frac{\Delta t}{\tau_{chem}})\phi(t^*) + (\frac{\Delta t}{\tau_{chem}})\phi^o. \tag{2}$$

In this equation $\phi(t^*)$ represents species mixing ratio at the intermediate time level t^* following the application of the photochemical sink/sources. τ_{chem} is a chemical relaxation timescale here chosen as 2 days in the troposphere and 6 hours above 1 hPa. Δt is the model timestep.

The choice of ozone and temperature climatologies in equation (1) can affect the quality of the ozone and weather forecasts in several ways. These climatologies are used for generating linear coefficients and for constraining the ozone distribution outside the stratospheric and UTLS domains. They also determine the ozone photochemical response to temperature and ozone perturbations, which is a fundamental issue with the use of ozone coupled models. The ozone prognostic equation in (1) shows that the photochemical term is particularly sensitive to the choice of climatologies. It can alter the interactions between ozone and temperature via unphysical contributions from the perturbation terms on the RHS of the equation. To solve these radiative and photochemical interactions, it is necessary to choose a set of ozone and temperature climatologies that represent a state of equilibrium representative of stratospheric conditions.

Climatologies can be built from different sources, including observations, reference models, and reanalyses. In this study, the original observation-based climatologies used by the LINOZ scheme have been replaced by a new set of climatologies generated from multi-year reanalyses. The use of reanalyses helps preserve the photochemical and radiative balance between ozone and temperature climatologies, which cannot generally be represented using observation-based datasets. With reanalyses, the ozone and temperature climatologies can be generated from the same dataset over the same domain and period, increasing the level of consistency between these two fields. The use

of reanalyses also allows for updating the ozone distribution by taking into account changes that have occurred over the past decades (WMO 2018).

Different types of reanalyses, such as ERA5 (Hersbach and Coauthors 2020), M2-SCREAM (Wargan et al. 2023), and CAMS (Inness et al. 2019), can be used to constrain the ozone linearized scheme throughout the stratospheric and tropospheric domains. The M2-SCREAM and CAMS assimilation systems provide a comprehensive set of chemical analyses that can be used to constrain the ozone distribution in various domains. The ERA5 system is based on a linearized ozone scheme but includes ozone as a model variable within the 4Dvar assimilation system. This approach contributes to preserving the coherence between the ozone and temperature analyses, which is an important element of the study.

In this study, we have chosen ERA5 reanalyses to maximize the consistency between ozone and temperature climatologies. The monthly mean ozone and temperature have been generated from the same datasets for the period 2010 to 2016. This period is relatively short but comparable to the period covered by other climatologies used in linearized schemes (Geer et al. 2007). In the lower mesosphere, from 1 hPa to 0.3 hPa, the ozone climatology is based on the Fortuin and Kelder (1998) reference model, whereas ozone measurements from the Halogen Occultation Experiment (HALOE) are used from 0.3 hPa to the model lid. The ozone climatology is interpolated on hybrid model levels via linear interpolation in log pressure coordinates.

b. Heterogeneous processes

The model includes a parameterization scheme for representing the photochemical reactions occurring on the surface of PSCs. The formulation is based on a cold tracer approach for determining the pre-conditioning phase of air masses (e.g. Cariolle and Teyssèdre (2007) and Geer et al. (2007)). According to these approaches, the degree of halogen activation is determined by a tracer β , which is used to parameterize the rate of ozone destruction, taking the following form:

$$\frac{d\phi}{dt}|_{het} = \frac{-1}{\eta}\beta\phi. \tag{3}$$

This expression is only applied in direct sunlight conditions using $\eta = 10$ days as a decaying time constant representative of the strength of the ozone depletion process. The prognostic equation for the cold tracer β is defined as:

$$\frac{d\beta}{dt} = \frac{1}{\eta_P}(1 - \beta) - \frac{1}{\eta_L}\beta \tag{4}$$

following Geer et al. (2007). The first term on the right hand side represents the activation process and is applied when the temperature is below a threshold value of 195K. η_P represents a characteristic activation timescale estimated as 4 hours. The second term represents the de-activation process and is applied in direct sunlight conditions with a time constant η_L of 10 days. β is reinitialized to nil at the beginning of each forecasts.

The ozone tendency in (3) is added after applying the gas-phase tendency in (1) using a process splitting approach. The parameterization scheme is applied in a restricted area between 12 km and 22 km based on a sensitivity study that indicated a slight overestimation of the ozone-depleted area when the original settings from Geer et al. (2007) were used. This specific choice of settings appears appropriate in the context of the very severe 2020 ozone depletion events. However, further evaluation is needed to ensure that the parameterization scheme can also represent the large interannual variability of ozone loss processes in both polar regions (Monge-Sanz et al. 2022).

3. Ozone assimilation

The GDPS assimilates both meteorological and ozone observations. Meteorological observations are assimilated using the ensemble–variational approach (Buehner et al. 2015), whereas a three-dimensional variational assimilation with a first-guess at the appropriate time is used for ozone assimilation (Rochon et al. 2019). This difference arises because ozone forecasting is not included in the system that generates the ensembles necessary for the ensemble-variational approach.

In this study, ozone retrievals from six satellite instruments are assimilated. The bulk of the data consists of retrieved integrated TOC values from the Ozone Monitoring Instrument (OMI) on board the AURA satellite (Bharthia and Wellemeyer 2002), the nadir mapping from the Ozone Mapping and Profiler Suite (OMPS-NM) on board the Suomi National Polar-orbiting Partnership (Suomi NPP) (Flynn et al. 2017), and measurements from the Tropospheric Monitoring Instrument (TROPOMI) on board Sentinel-5 (Garane et al. 2019). The assigned observation error standard deviation for OMI and OMPS-NM data is set from a single iteration of the Desroziers et al. (2005)

approach, with verification and adjustment from the standard deviation of differences from colocated OMI and OMPS-NM data. Those for TROPOMI are as provided with the level 2 data.

Ozone data from three profiler instruments are also assimilated, including measurements from the Microwave Limb Sounder (MLS) on board AURA, measurements from the Backscatter Ultraviolet second-generation Instrument (SBUV/2) on board NOAA-19, and measurements from the Nadir Profiler of the Ozone Mapping and Profiler Suite (OMPS-NP) on board Suomi NPP. MLS retrieved concentration profiles are most effective in constraining and preserving the quality of the ozone field's vertical structure. It provides data under both daytime and nighttime conditions, while all others only provide daytime data. The influence of the SBUV/2 and OMPS-NP retrieved partial column profilers is currently weak, even more so for the latter which remains to be resolved. References on retrievals for the profiler data are summarized in McPeters et al. (2013) for SBUV/2 and Bai et al. (2016) for OMPS-NP. The applied observation error standard deviation of the profiles is currently those provided with the retrieval products.

The 21 layers of the original partial column profiles are reduced to six thicker, potentially usable layers, as these profiles contain the equivalent of at most about four pieces of independent information. The corresponding retrieved measurement averaging kernels are applied in the assimilation. The roughly four pieces of independent information denote the reduced degree of freedom resulting from the correlation of the original layers, as seen through the overlapping averaging kernels of the retrieved measurements. The thicker layers are generated by combining neighboring original layers. The result is a set of layers that are less correlated with each other through their averaging kernels, except for the strongly coupled bottom two layers. The specified layer boundaries are 0.101, 1.01, 2.54, 6.38, 25.43, 254.3 hPa, and the surface.

4. Chemical data assimilation experiments

The ozone coupled GDPS was evaluated during the 2020 Northern Hemisphere (NH) and Southern Hemisphere (SH) ozone hole events. The system produced weather and ozone analyses every 6 hours, while 10-day forecasts were launched every 12 hours at a 25 km resolution throughout both springtime periods. The assimilation cycle was based on a model version that included ozone radiative coupling but did not include the parameterization of heterogeneous chemistry. Past experiments with the GDPS system have shown that the impact of the parameterization scheme on

the quality of ozone analyses is not significant with the use of a 6-hour assimilation window. This is attributed to the fact that the number of observations used by the assimilation system is generally large enough to produce a realistic representation of the ozone hole throughout the entire springtime period.

The weather and ozone analyses produced by the GDPS system serve as initial conditions for all forecast experiments. They also serve to evaluate the quality of the forecasts at different lead times. All experiments consist of launching a single 10-day forecast every 12 hours throughout both springtime periods. In this study, forecast experiments with and without the heterogeneous parameterization scheme have been performed to evaluate the impact of those reactions on ozone predictability. Further experiments with and without ozone radiative coupling have been performed to evaluate the radiative impact of ozone on the quality of the weather forecasts.

a. Ozone forecasting

1) SOUTHERN HEMISPHERE

In 2020, the ozone hole over Antarctica was one of the strongest on record in terms of size and depth (Blunden, 2021). It was also one of the longest lasting events, with the breaking of the vortex occurring at the end of December. During this period, the minimum Total Ozone Column (TOC) was diagnosed daily to evaluate the capability of the heterogeneous chemistry parameterization to deplete ozone below the 220 DU threshold, which is considered the minimum value that can be obtained from dynamical processes.

Figure 1 shows the evolution of the TOC minimum between the 40°S and 90°S latitude bands from August 1st to the end of December 2020. Results are diagnosed from the GDPS analyses, the Copernicus Atmosphere Monitoring Service (CAMS) reanalyses (Inness et al. 2019), and measurements from the OMPS instrument onboard the Suomi NPP satellite, taken from the NASA Ozone Watch website at https://ozonewatch.gsfc.nasa.gov. The minimum value is picked within a wide latitude band for all the datasets to ensure that the diagnostic is applied throughout the whole area of the polar vortex for the entire event. Data reveal that both analysis systems effectively capture the ozone behavior from the ozone-hole formation period to the recovery period beginning in early October. From August to mid-September, the OMPS values are significantly lower than GDPS and CAMS, which could be partially attributed to the limited amount of ozone
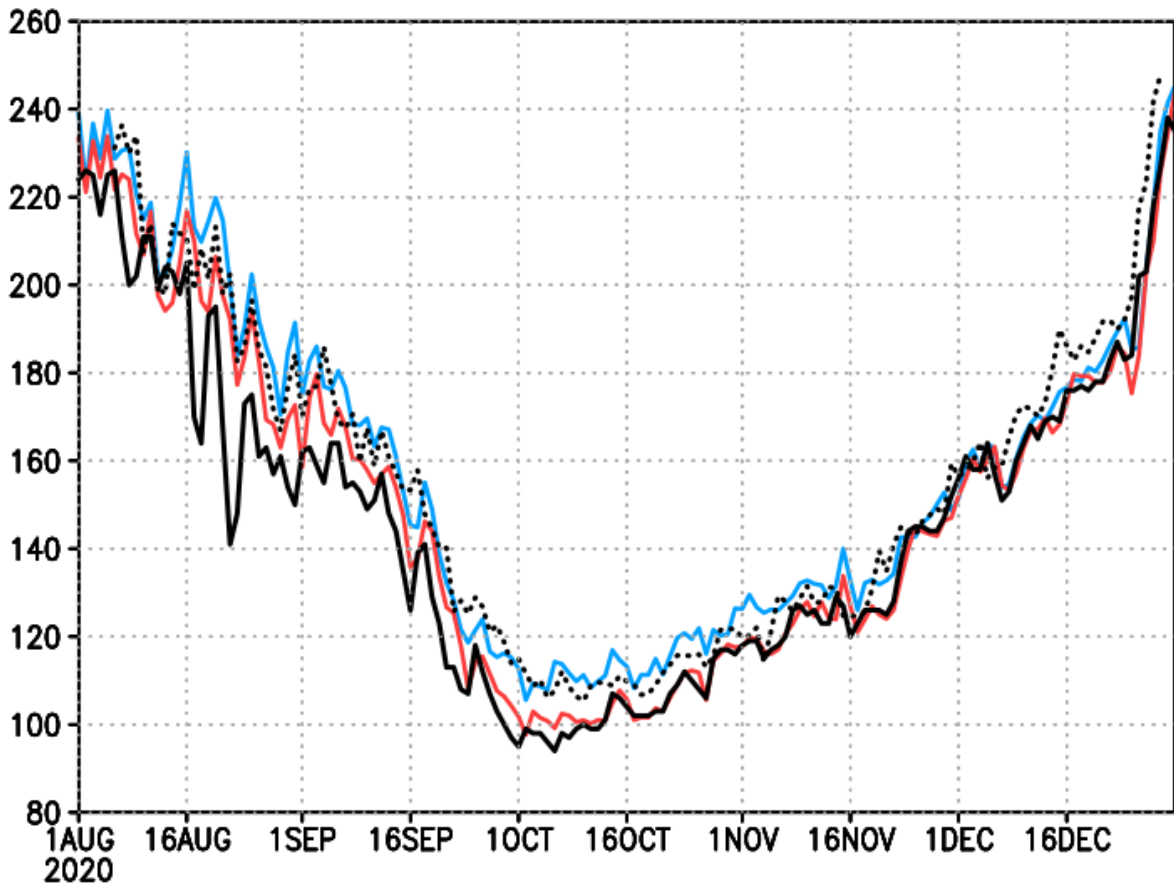
FIG. 1: Time Series of the TOC minimum (DU) from August 1st to December 31th 2020 within the $40°$S and $90°$S latitude bands. From GDPS analyses (red), CAMS reanalyses (blue), observations from NASA Ozone Watch (black) and GDPS forecast at 5-day lead time (black dotted line)

observations that can be assimilated over the period in the absence of sunlight. Following this period, there is good agreement between the GDPS analyses and the OMPS instrument, whereas the ozone minimum from CAMS is slightly higher.

The differences observed in the timeseries between the GDPS and CAMS can be attributed to various assimilation and modeling aspects. The CAMS reanalysis system is based on a model that includes the parameterization of heterogeneous reactions (Cariolle and Teyssèdre 2007), whereas the GDPS assimilation cycle is based on a model version that does not include such processes. Nevertheless, the GDPS system produces lower ozone values, highlighting that the differences observed throughout the period are likely associated with the ozone assimilation process. The use of a bias correction scheme in the CAMS system, but not in the GDPS, is one factor that could produce systematic differences between both assimilation systems.

Figure 1 also presents the results from the forecast experiment at a 5-day lead time using a model version that includes the parameterization of heterogeneous reactions. It indicates that the differences between the ozone forecasts and analyses generally remain under 10 DU, which is within the analysis uncertainties estimated from the differences between the GDPS and CAMS analyses.

Throughout August and September, the ozone forecasts are in general agreement with analyses, indicating that the parameterization scheme provides a reasonable estimation of the ozone loss process. During October, the ozone forecast systematically overestimates the ozone minimum, which can be attributed to numerical effects such as model resolution, which may not be sufficient to preserve the TOC minimum values present in the analyses. In November and December, the ozone layer recovers rapidly due to the mixing of ozone-depleted air within the polar vortex with ozone-rich air from the mid-latitudes. This large-scale process appears to be reasonably represented by the model, even though the model overestimates the ozone recovery associated with the final breakup of the polar vortex in December.

In Figure 2, the experiment is compared against a control in which the ozone forecasts were launched without including the parameterization of heterogeneous reactions. The left panels present the time evolution of TOC mean bias (%) evaluated against the GDPS analyses over the Antarctic region at different forecast lead times. The figure shows that the experiment without the parameterization scheme suffers from a significant bias, which is particularly important during the ozone hole formation period when the strength of the chemical ozone loss maximizes. Results indicate that the mean bias throughout the entire period increases linearly from 3% at a 3-day lead time to about 10% at a 10-day lead time. With the inclusion of heterogeneous chemistry, the mean bias decreases significantly and remains under 2% for all lead times. This result suggests that the choice of ozone depletion lifetime in the heterogeneous parameterization scheme is slightly more appropriate for capturing the strength of the loss rate at longer timescales. During the vortex closure period starting from mid-October, the impact of the photochemistry is smaller, and both experiments give similar results.

The right panels in Figure 2 present the time evolution of TOC standard deviation over the region.
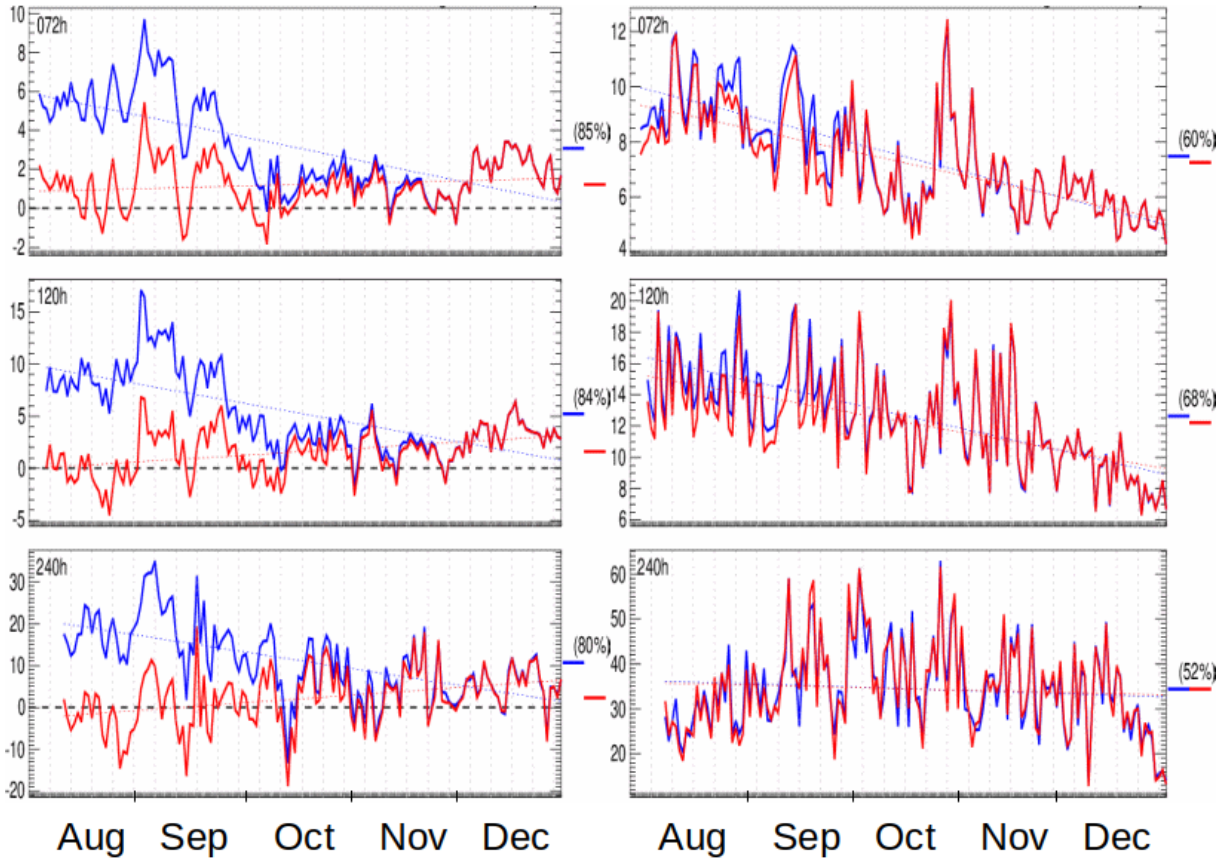
FIG. 2: Time Series of TOC mean differences (left) and standard deviation (right) in (%) between forecasts and GDPS analyses in the 60°S and 90°S latitude bands at 70 hPa. Ozone forecasts at 3-5-10-day lead times are from the experiments with (red) and without (blue) the parametrization of heterogeneous chemistry. Marks on the right axis denote the mean differences (%) and the number in brackets denotes the percentage of forecasts for which the differences are larger for the experiment without the parameterization scheme. The dotted lines are the linear regression that best fits the data of both experiments.

The standard deviation appears larger in the early stages of the event and decreases progressively over time. This trend is particularly significant at a 5-day lead time, showing a constant decline in the standard deviation from about 16% in early August to 8% at the end of December. This systematic reduction is attributed to a better representation of dynamical processes as we progress toward the vortex breakup period. In August and September, the TOC standard deviation is slightly improved due to the inclusion of heterogeneous chemistry. During the ozone recovery period from mid-October, the impact of the parameterization scheme on the standard deviation is not significant, and the model errors appear mainly determined by the representation of dynamical
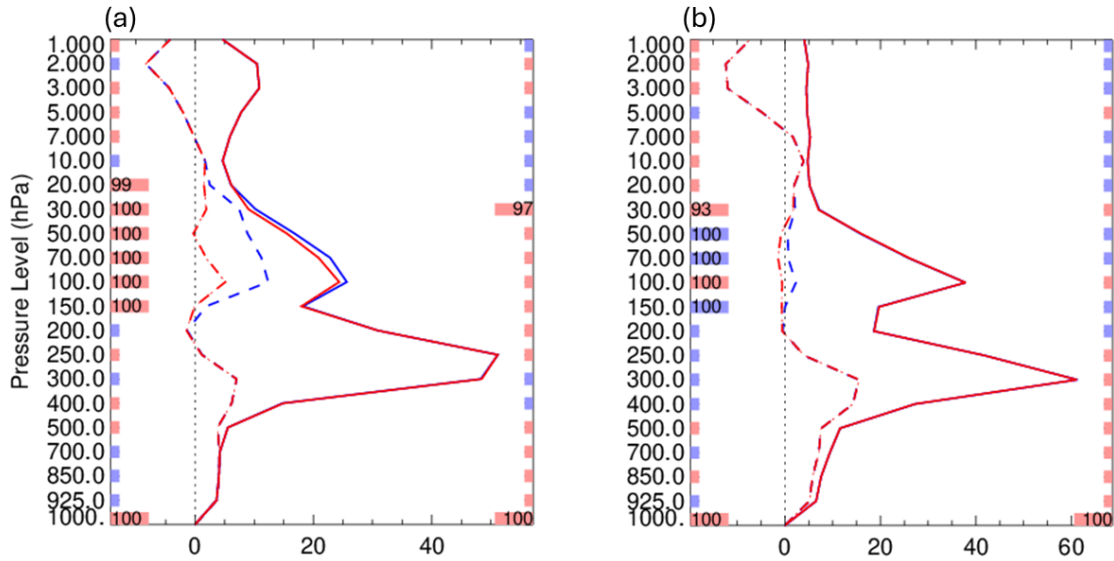
FIG. 3: Five-day ozone forecasts against GDPS analyses (%) within the 60°S and 90°S latitude bands from (a) August 1st to September 30th 2020 and (b) October 1st to December 31th 2020. Ozone forecasts are from the experiments with (red) and without (blue) the parametrization of heterogeneous chemistry. Dash lines are the mean and solid lines are the standard deviation. Boxes on the left (right) denote statistical significance levels for the bias (standard deviation) computed using permutation tests (see chapter 15 of Efron and Tibshirani (1994)). Red (blue) boxes mean that the experiment which includes the parameterization scheme is better.

processes, which could be improved with the use of higher resolution models. Results also reveal that the standard deviation decreases significantly at all lead times in late December, indicating that the GDPS can capture the final breakup of the polar vortex. At the 10-day lead time, the standard deviation is relatively constant regardless of the processes involved, suggesting that the gain of predictability obtained from model developments will likely be reduced at those timescales.

The overall impact of the heterogeneous chemistry parameterization scheme on the ozone forecasts at a 5-day lead time over Antarctica is presented in Figure 3. From August to September (left panel), the results show a statistically significant reduction of the mean ozone bias by about 10% throughout the lower stratosphere. The figure also shows a systematic decrease in the ozone standard deviation below 30 hPa, reaching an average of 2% in the lower stratosphere. This reduction does not appear significant at the 95% confidence level but is observed throughout the lower stratosphere, where the temperature of the polar vortex is cold enough for the generation of
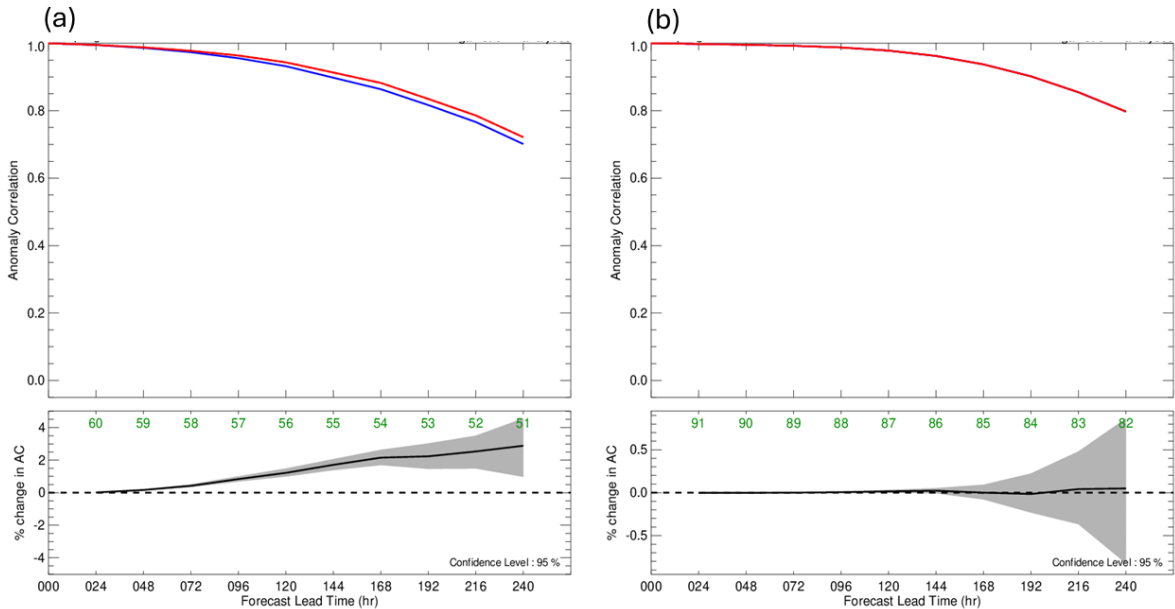
FIG. 4: Anomaly Correlation Coefficient of TOC for the period (a) August 1st to September 30th 2020 and (b) October 1st to December 31th 2020 as a function of lead times (in hours) within the 60°S and 90°S latitude bands. Ozone forecasts are from the experiments with (red) and without (blue) the parametrization of heterogeneous chemistry. Digits in green represent the number of forecasts used in the calculation at the given lead time. The bottom panel shows the differences between both experiments whereas the shading indicates the 95% confidence level. Confidence limits are obtained from bootstrapping the adjusted correlation coefficient after applying a Fisher transformation to convert the correlation coefficient to a normally distributed variable. This process involves repeatedly resampling the data with replacement.

PSCs. Results show that the ozone standard deviation is very large in the tropopause region, which may indicate the limitations associated with the use of a linearized stratospheric model at those altitudes, as discussed later in section 4a.2. From October to December (right panel), the ozone bias and standard deviation increase throughout most of the lower stratosphere, which can be attributed to the large dynamical variability of the polar vortex. The signal is statistically significant throughout the region, but the impact of the parameterization scheme on the quality of the ozone forecast is generally neutral throughout this period.

The ozone predictability in the lower stratosphere can be estimated by comparing TOC forecasts and analyses using ACC. The computation of ozone anomalies is done at every 24-hour lead time and makes use of the ERA5 ozone climatology as the reference dataset. Figure 4a presents the TOC predictability during the ozone hole formation period from August to September when the
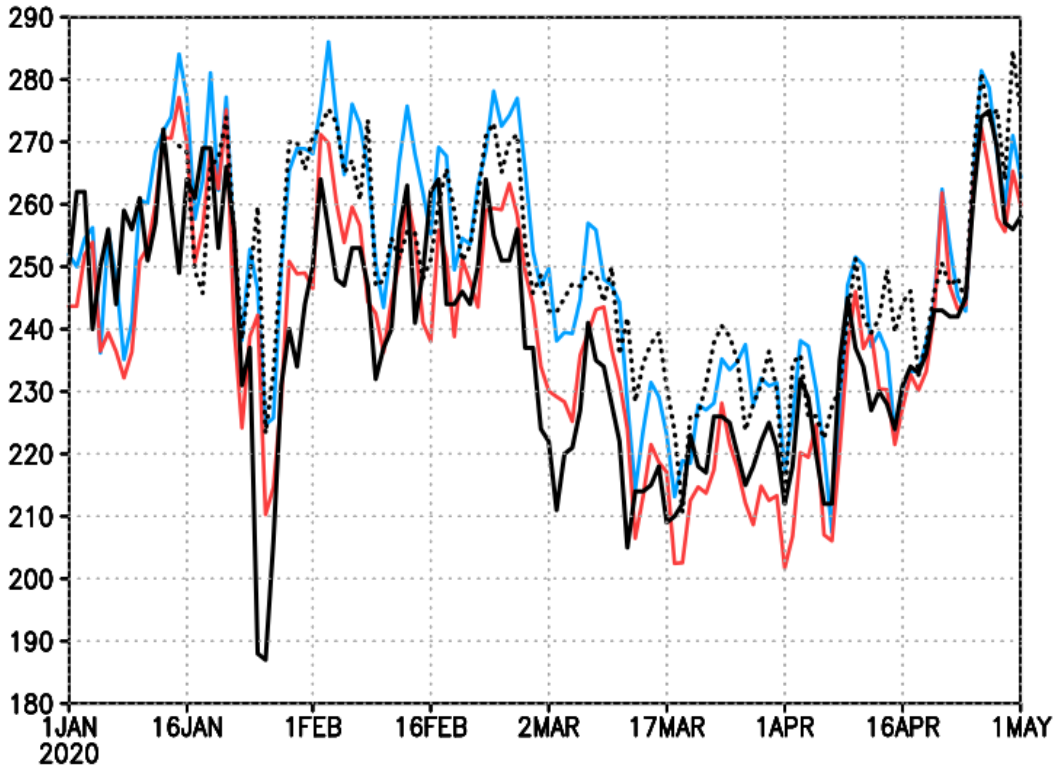
17

FIG. 5: Time Series of the TOC minimum (DU) from January 10th to April 30th 2020 within the 60°N and 90°N latitude bands. From GDPS analyses (red), CAMS reanalyses (blue), observations from NASA Ozone Watch (black) and GDPS forecast at 5-day lead time (black dotted line)

quality of the forecast is largely controlled by photochemical processes. The results show that the inclusion of the parameterization scheme increases the TOC predictability at all lead times during this period. After 10 days, the ACC difference reaches 0.04, which corresponds to a gain of predictability of about 8 hours, statistically significant at the 95% confidence level as denoted on the bottom panel. This highlights the reduction of modeling errors associated with the use of the parameterization scheme. The ozone predictability during this period exceeds 10 days using the 0.6 ACC reference value as a benchmark. This estimation is significantly larger than other values found in the literature (Sekiyama and Shibata 2005; Eskes et al. 2002; Stajner et al. 2006), highlighting the progress made in the performance of operational NWP systems over the past decades. Figure 4b shows that during the vortex closure period starting in October, the ACC value increases from 0.7 to 0.8 at a 10-day lead time, which corresponds to a gain of predictability of about 1 day. Throughout this period, the predictability of TOC is comparable to the predictability of temperature at 70 hPa shown on Figure 10.

18

2) NORTHERN HEMISPHERE

The system has been evaluated in the northern polar region during the late winter and spring periods of 2020, when the temperature stayed below the PSC threshold value for several weeks. The large spatio-temporal variability of the region provides suitable conditions for assessing ozone predictability in a dynamical regime where chemical loss rates are relatively small compared to the SH.

Figure 5 shows the evolution of the TOC minimum between the 60°N and 90°N latitude bands from January 10th until the end of April 2020. Results are diagnosed as previously from the GDPS analyses, the Copernicus Atmosphere Monitoring Service (CAMS) reanalyses, and measurements from the OMPS instrument onboard the Suomi NPP satellite, taken from the NASA Ozone Watch website. During this period, both sets of analyses reproduce the strong day-to-day variability, with minimum ozone values just above 200 DU towards the second half of March. The mean minimum value in March from the GDPS, at approximately 215 DU, is lower than CAMS by almost 10 DU but is in general agreement with OMPS and measurements from the TROPOMI instrument onboard the Sentinel 5 satellite during the same period (Dameris et al. 2021). The forecasts at a 5-day lead time shown in Figure 5 appear slightly biased against the GDPS analyses but remain within the range of analysis uncertainties. As discussed previously on Figure 1 this systematic overestimation of the ozone minimum could be partially attributed to a model resolution issue.

The comparison against the control experiment, which doesn't include the parameterization of heterogeneous reactions, is shown in Figure 6. The results highlight a significant reduction of the mean biases at all lead times associated with the use of the parameterization scheme. The impact is particularly important in March, where the TOC bias at a 5-day lead time is reduced by half with the inclusion of the parameterization scheme. The mean bias for the full period is 2% at a 3-day lead time and 3% at a 10-day lead time, indicating that the heterogeneous chemistry scheme produces a better estimation of the ozone loss rates at longer timescales, as seen in the SH. Figure 6 shows that the TOC standard deviation is larger than it is over Antarctica, which is associated with the large dynamical variability of the region. The results also show a few percent reduction of the standard deviation in March directly associated with the inclusion of the parameterization scheme.

The ozone predictability from January to April remains high and doesn't increase significantly when the parameterization of heterogeneous chemistry is included, as it occurs in the SH. This
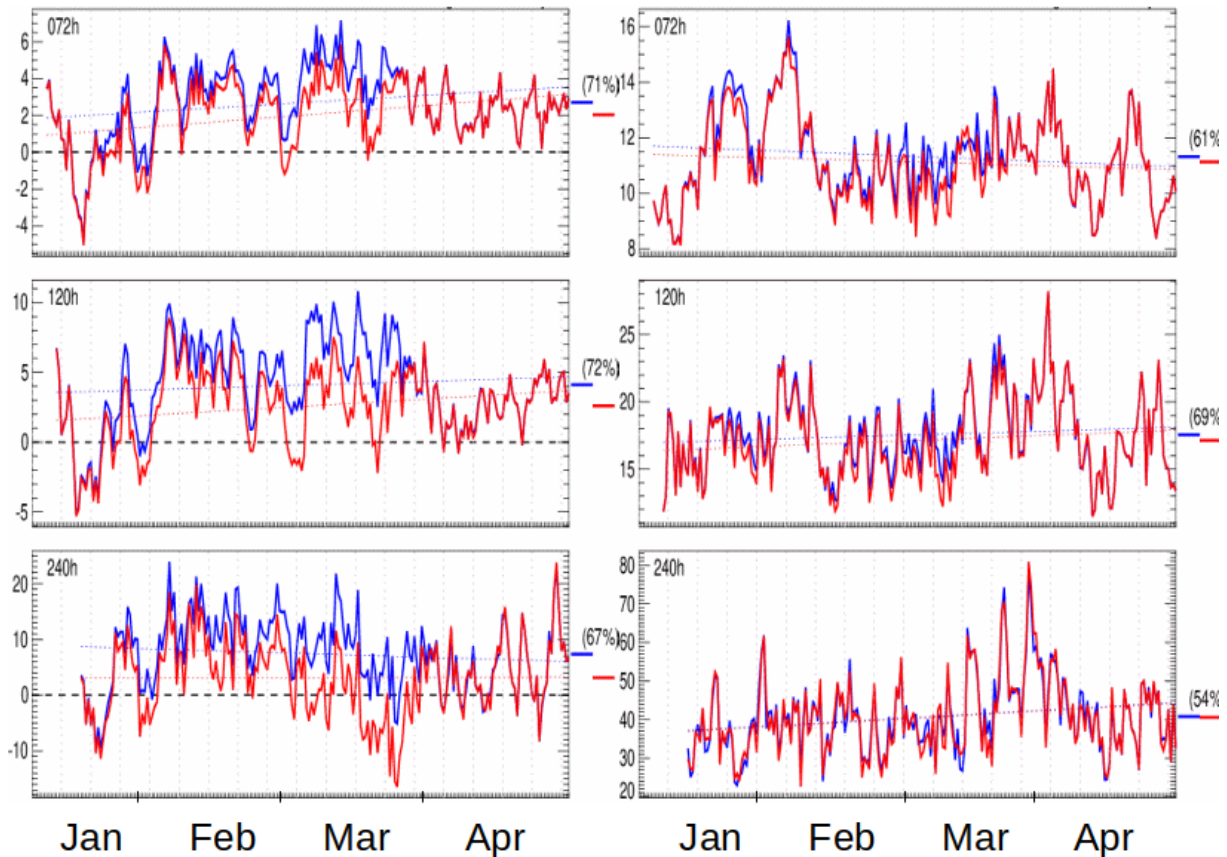
FIG. 6: Time Series of TOC mean differences (left) and standard deviation (right) in (%) between forecasts and GDPS analyses in the 60°N and 90°N latitude bands at 70 hPa. Ozone forecast at 3-5-10-day lead times from the experiments with (red) and without (blue) the parametrization of heterogeneous chemistry. Marks on the right axis denote the mean differences (%) and the number in brackets denotes the percentage of forecasts for which differences are larger for the experiment without the parameterization scheme. The dotted lines are the linear regression that best fits the data of both experiments.

is likely associated with the smaller magnitude of the ozone loss process and the relatively short period in which this photochemical process is active. Figure 7a shows that the TOC ACC value reaches 0.8 after 10 days, which is comparable to the value obtained during the ozone recovery period in the SH shown previously in Figure 4b. ACC results also indicate that the TOC predictability is systematically lower than the temperature predictability at 70 hPa in both hemispheres and decreases faster with time throughout the lower stratosphere. This is attributed to the fact that TOC is an integrated quantity, which is strongly influenced by the ozone distribution in the lowermost stratosphere between 100 hPa and the tropopause, where most stratospheric-tropospheric exchange processes take place (Holton et al. 1995).
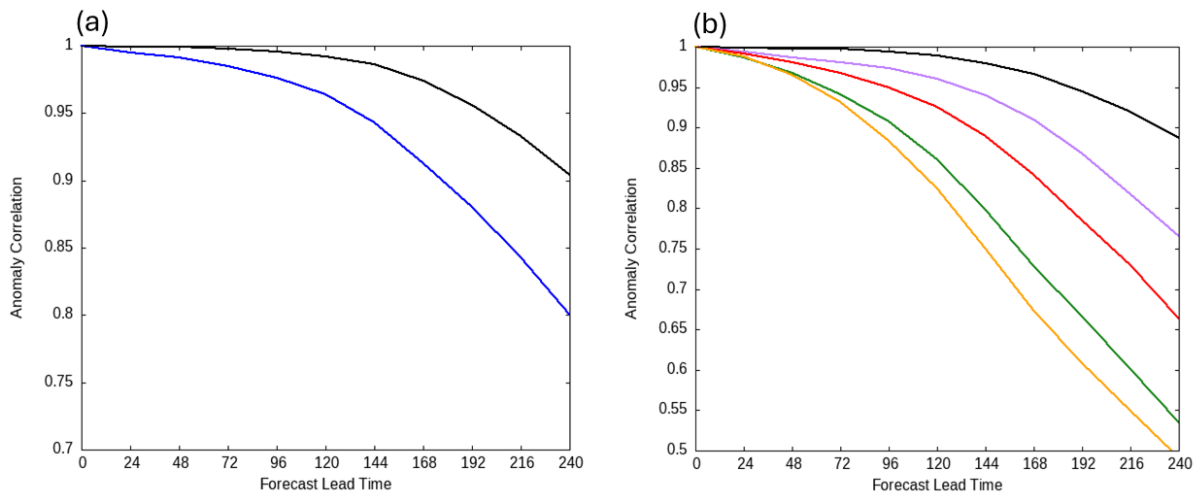
FIG. 7: Anomaly Correlation Coefficient as a function of lead times (in hours) within the 60°N and 90°N latitude bands for the period January 10th to April 29th 2020 from the experiment with the parametrization of heterogeneous chemistry. (a) Temperature at 70 hpa (black) and TOC (blue). (b) Temperature at 100 hPa (black) and ozone at 50 hPa (purple), 70 hPa (red), 100 hPa (green) and 200 hPa (orange)

Figure 7b shows that ACC values evaluated from the ozone mixing ratio decrease rapidly below 70 hPa, whereas the temperature predictability (in black) remains very high throughout the UTLS region. This rapid decrease in ozone predictability appears at all latitudes (not shown), highlighting the limitations associated with the use of a stratosphere linearized scheme in regions potentially affected by mass fluxes originating from the troposphere. Results show that the TOC predictability is larger than the ozone predictability evaluated at specific pressure levels, indicating that TOC remains a valuable metric for evaluating the overall performance of the ozone forecasting system. The ozone predictability below 70 hPa could be improved using higher resolution forecasts and a more comprehensive photochemical scheme. The assimilation of additional limb sounding measurements (e.g. Flynn et al. (2006)) would also contribute to improving the quality of ozone analyses throughout the region.

b. Ozone radiative coupling

Throughout springtime periods, the impact of ozone heating on the evolution of the polar vortices can be significant in both hemispheres (Monge-Sanz et al. 2022; Oh et al. 2022). In such conditions, the standard approach of using monthly mean ozone distributions for the computation of heating rates can generate a systematic overestimation of solar heating, as demonstrated
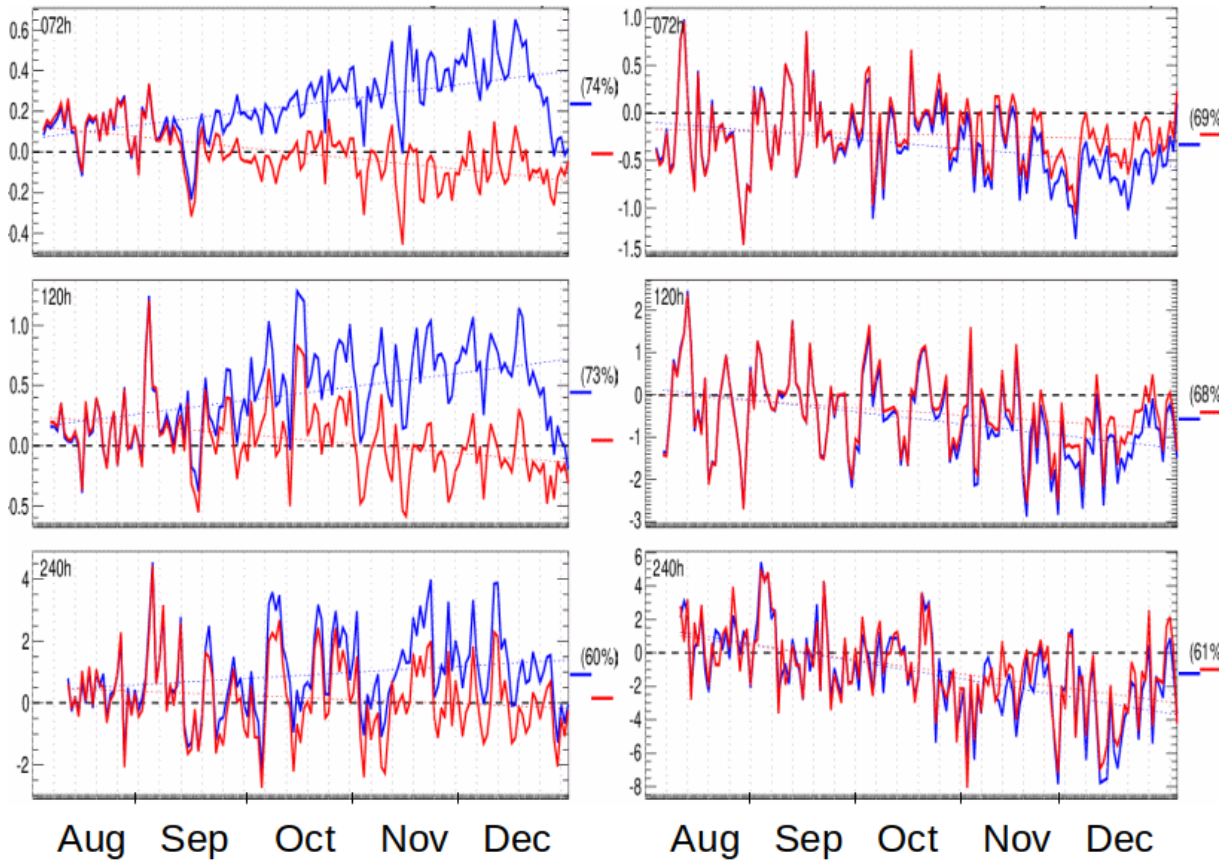
FIG. 8: Time Series of temperature (left) and zonal wind (right) mean differences between forecasts and GDPS analyses in the 60°S and 90°S latitude bands at 70 hPa. Weather forecast at 3-5-10-day lead times from the experiments with (red) and without (blue) the inclusion of ozone radiative coupling. The Y-axis shows differences in degrees (left panel) and m/s (right panel). Marks on the right axis denote the mean differences (%) and the number in brackets denotes the percentage of forecasts for which the differences are larger for the uncoupled experiment. The dotted lines are the linear regression that best fits the data of both experiments.

in Gillet et al. (2009) and Crook et al. (2008). Furthermore, this temperature bias can increase throughout the springtime period as solar forcing becomes more important and the polar vortex becomes more perturbed and drifts further away from zonal mean conditions.

The impact of ozone heating on medium-range weather forecasts in the polar regions can be evaluated by comparing an ozone-coupled experiment with a control cycle in which the ozone monthly mean climatologies are used for the computation of the heating rates. Figure 8 (left panels) shows the impact of ozone heating on the mean temperature forecasts at 70 hPa over the Antarctic region at different lead times.
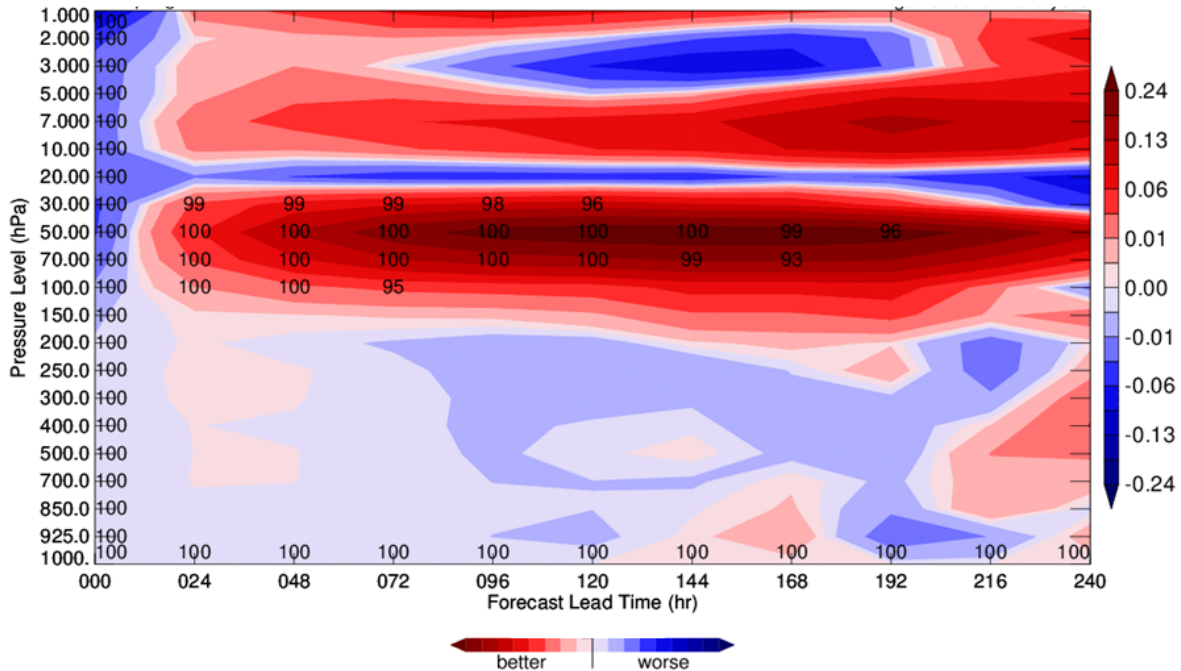
FIG. 9: Temperature standard deviation differences between forecasts and GDPS analyses as a function of lead time in the 60°S and 90°S latitude bands for the October-December 2020 period for the experiments with and without ozone coupling. Better results using the ozone coupled model (red) and better results using climatological ozone (blue). Numbers represent the confidence level computed using permutation tests (see chapter 15 of Efron and Tibshirani (1994)).

The timeseries indicate that the radiative impact of ozone starts to become significant around mid-September and increases steadily until the final breakup of the polar vortex. Prior to that period, solar heating rates are relatively small, which mainly explains the weak impact of ozone on temperature forecasts. In November and December, the solar fluxes reach their maximum intensity while the polar vortex becomes highly perturbed. Results show that throughout this period, the differences increase with forecast lead times by about 0.1 K/day with the use of prognostic ozone. This contributes to eliminating most of the warm temperature bias present in the control experiment at all lead times.

Figure 8 (right panels) reveals that the associated cooling intensifies the strength of the polar vortex through thermal wind balance. It contributes to reducing the zonal wind bias, which is particularly significant throughout the vortex closure period in December. The impact on the mean temperature and mean zonal wind fields is statistically significant and represent a significant fraction of the standard deviation as shown in Figure 13.
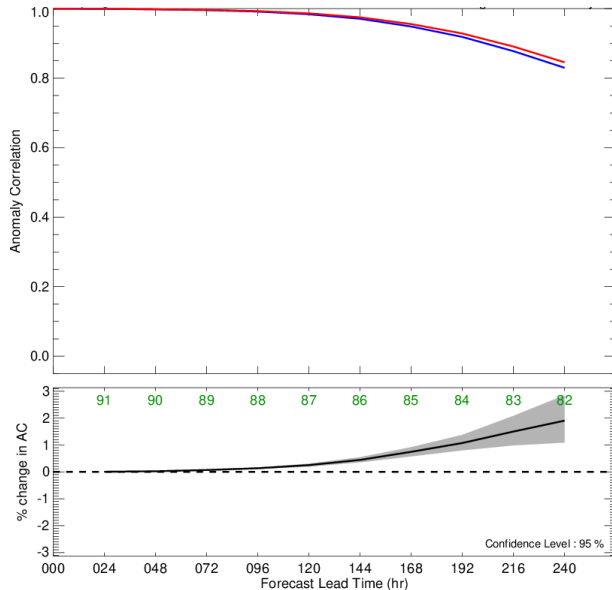
23

FIG. 10: Temperature anomaly correlation at 70 hPa within the 60°S and 90°S latitude bands for the period October-December 2020 as a function of lead times from the experiments with (red) and without (blue) the inclusion of ozone radiative coupling. Digits in green represent the number of forecasts used in the calculation at the given lead time. The bottom panel shows the differences between both experiments whereas the shading indicates the 95% confidence level. Confidence limits are obtained from bootstrapping the adjusted correlation coefficient after applying a Fisher transformation to convert the correlation coefficient to a normally distributed variable. This process involves repeatedly resampling the data with replacement.

The timeseries in Figure 8 also indicate that the impact of the heterogeneous chemistry parameterization scheme on the quality of weather forecasts at medium-range timescales is relatively small. Results indeed show that the temperature signal is minimal in August and September when the parameterization scheme is effective, whereas the temperature signal increases significantly from early October once the ozone hole is formed. These results suggest that the improvement in the temperature and wind forecasts is linked to the representation of the ozone advection process and the quality of the ozone analyses, which mainly determined the quality of the ozone forecast and associated radiative forcing during the ozone recovery period from early October.

During the ozone recovery period from early October, the temperature standard deviation between the forecast and the analyses decreases systematically throughout the stratosphere with the use of the ozone coupled model. Figure 9 compares the mean differences between the temperature standard deviation from both experiments at all lead times throughout the model domain. It shows that the largest impact on the temperature forecasts occurs in the lower stratosphere, where the ozone distribution is far from zonal mean conditions. Results indicate that the reduction of the
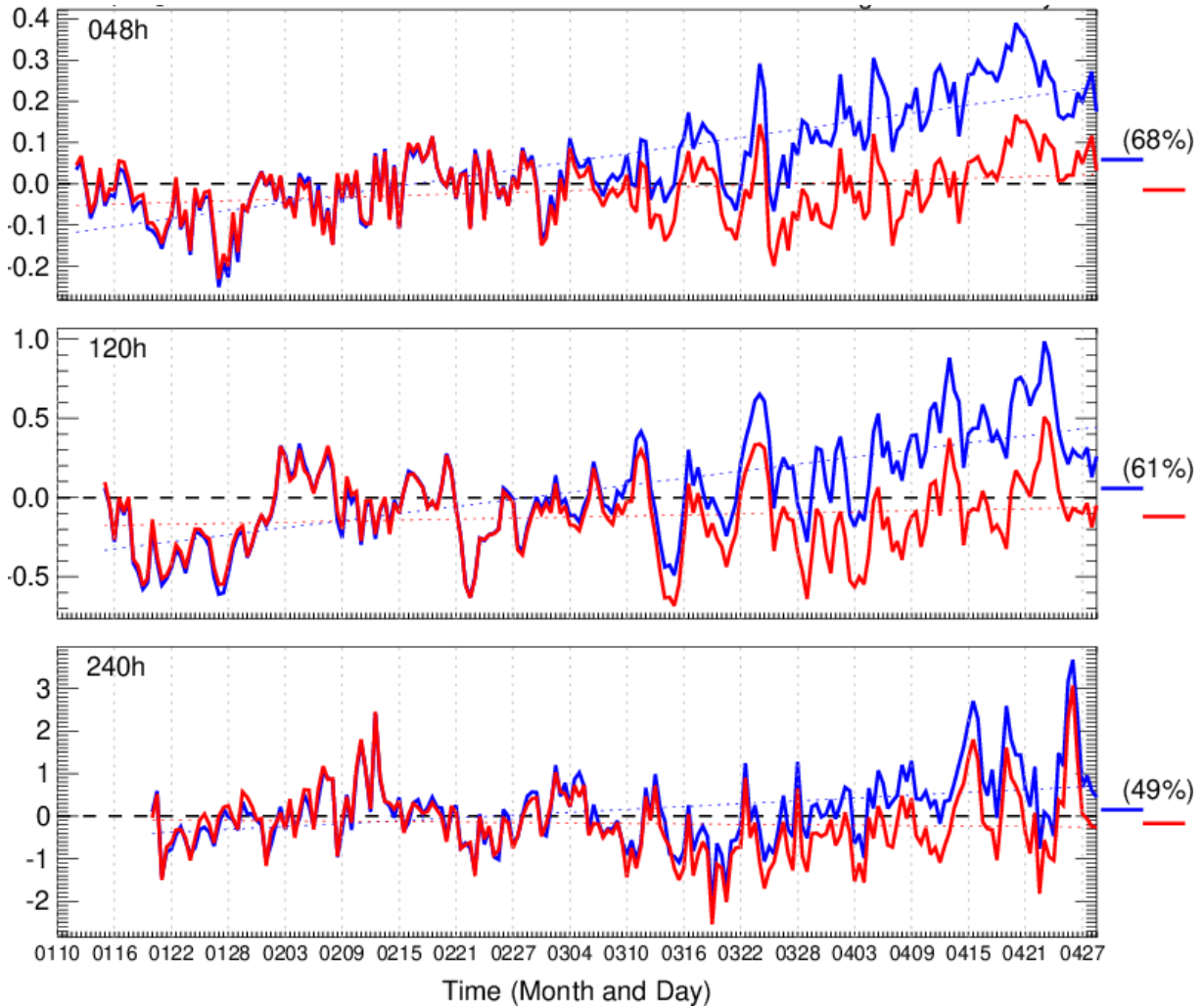
24

FIG. 11: Time Series of temperature mean differences (degrees) between forecasts and GDPS analyses in the 60°N and 90°N at 70 hPa. Weather forecast at 3-5-10-day lead times from the experiments with (red) and without (blue) the inclusion of ozone radiative coupling. Marks on the right axis denote the mean differences (%) and the number in brackets denote the percentage of forecasts for which the differences are larger for the uncoupled experiment. The dotted lines are the linear regression that best fits the data of both experiments.

mean temperature standard deviation exceeds 0.2 degrees at 50 hPa and maximizes between 4-day and 8-day lead times.

The temperature response shown in the previous figures can be compared with published results from Monge-Sanz et al. (2022). This study shows annual mean temperature differences that can reach 1°at a 10-day lead time in the lower stratosphere extra-tropical regions, which is comparable to the signal seen in Figure 8. Their study also indicates that the temperature signal in the Southern
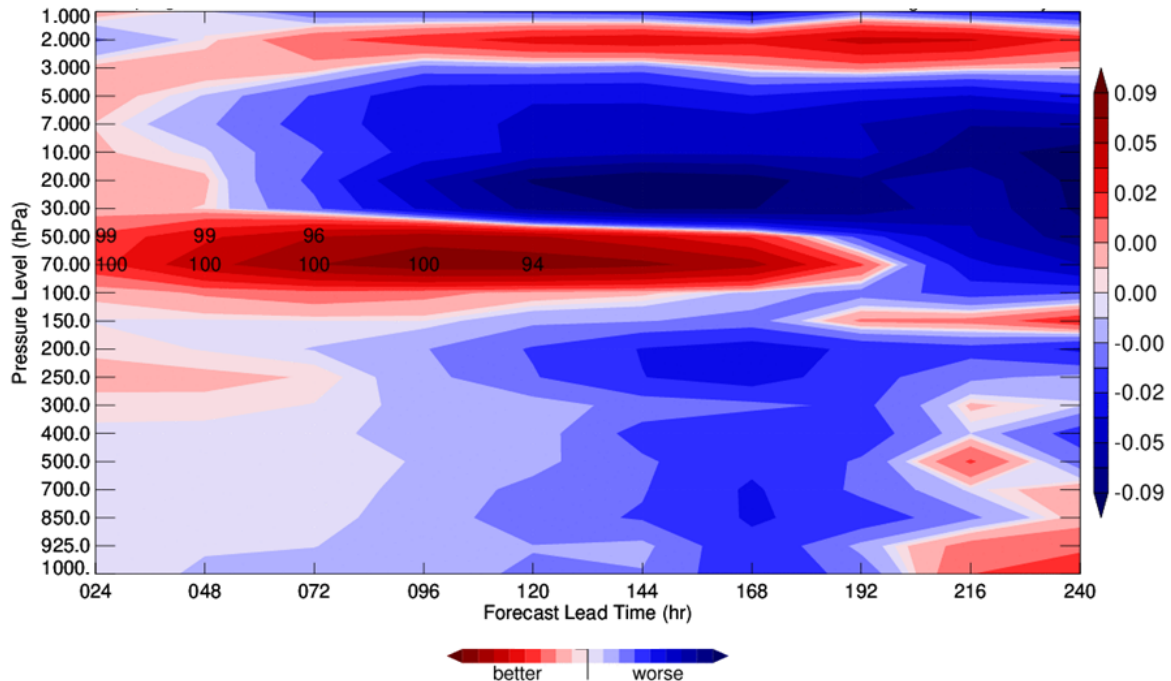
FIG. 12: Temperature standard deviation differences between forecasts and GDPS analyses as a function of lead time in the $60°N$ and $90°N$ latitude bands from January 10th to April 29th 2020 for the experiments with and without ozone coupling. Better results using the ozone coupled model (red) and better results using climatological ozone (blue). Numbers represent the confidence level computed using permutation tests (see chapter 15 of Efron and Tibshirani (1994)).

Hemisphere maximizes around the 5-day lead time, similar to the signal shown in Figure 9. This may suggest some radiative adjustment of the temperature beyond that timescale in the region.

Figure 10 shows that the temperature anomaly correlation at 70 hPa over the Antarctic region increases significantly at all forecast lead times during this period. The impact is particularly notable beyond the 3-day lead time, where the signal exceeds the 95% confidence level. This result shows that temperature predictability is relatively high in the region and increases by almost half a day at the 10-day lead time with the use of the ozone-coupled model, indicating a significant improvement in forecast errors throughout the event.

Over the Arctic, the radiative impact of ozone is generally smaller but remains notable. The temperature signal maximizes during March-April when solar heating becomes significant over the region. Figure 11 shows that the model suffers from a warm bias over the Arctic, which is reduced with the use of a prognostic ozone representation. The signal remains significant until the
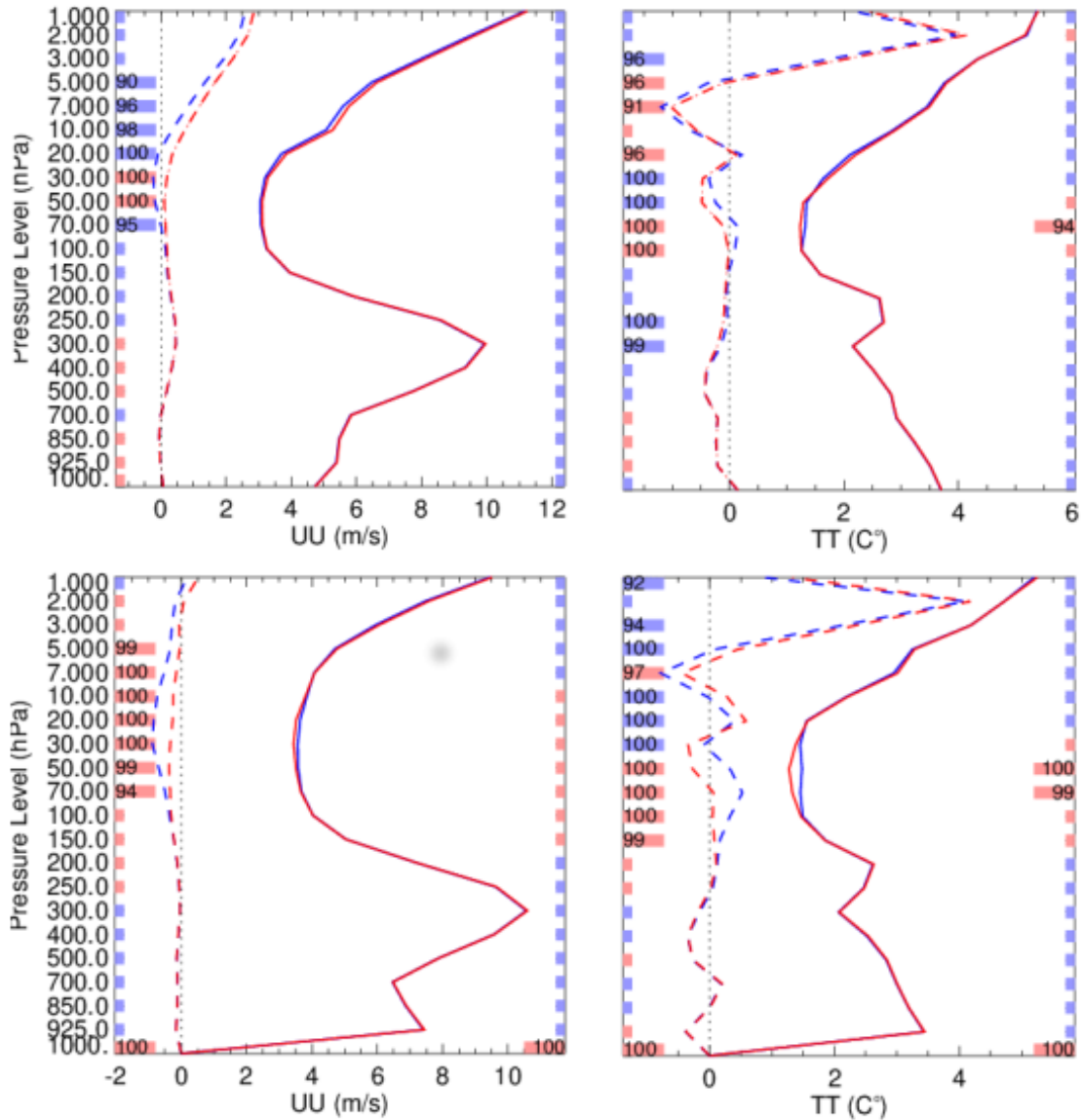
FIG. 13: Five-day weather forecasts against GDPS reanalyses in the 60°N and 90°N latitude bands (top panels) and 60°S and 90°S latitude bands (bottom panels) for the zonal wind (left) and temperature (right) from the experiments with (red) and without (blue) the inclusion of ozone radiative coupling. Dashed lines are mean biases while solid lines are error standard deviation. Boxes on the left (right) denote statistical significance levels for the bias (standard deviation) computed using permutation tests (see chapter 15 of Efron and Tibshirani (1994)). Red (blue) boxes mean that the ozone coupled (uncoupled) experiment is better.

end of April, which is due to the very unusual persistence of ozone-depleted air masses within the

Arctic vortex throughout the period (Manney et al. 2020).

Figure 12 also shows a decrease in the mean temperature standard deviation throughout the period. The reduction is statistically significant throughout the lower stratosphere and reaches 0.1 degrees around 70 hPa. The radiative impact of ozone decreases faster than in the Southern Hemisphere and doesn't last beyond the 8-day lead time. It is noted that the increase in the standard deviation in the upper stratosphere is not statistically significant at the 95% confidence level.

The overall benefit of using an ozone coupled model for weather forecasting in both polar regions is shown in Figure 13. The results indicate that the temperature forecasts at a 5-day lead time are significantly colder throughout the lower stratosphere in both polar regions, stemming from a better representation of the ozone loss process. In the SH, the weather forecasts are generally improved with a more intense and colder polar vortex in better agreement with the analyses. The standard deviation is also improved throughout the lower stratosphere, and the signal exceeds the 95% confidence level in the case of temperature. In the NH, the model response is similar, with a colder polar vortex and stronger zonal wind throughout the springtime period. In this case, the departure between the analyses and the forecasts has slightly increased throughout most of the stratosphere, which can be associated with the strengthening of the Brewer-Dobson Circulation. This shows the model's limitation in comprehensively resolving the nature of the momentum forcings and interactions involved.

5. Conclusions

The use of ozone as a prognostic constituent can improve NWP systems in several ways. It is a well-observed constituent that can be used as a valuable metric for evaluating the quality of medium-range weather forecasts throughout the stratosphere. The prognostic ozone distribution can also be used for the computation of heating rates, which further contributes to improving the predictability of large-scale weather variables. The impact of including ozone radiative coupling is particularly important in polar regions where the zonal asymmetries of the ozone distribution represent a significant element of the radiative forcing.

In this study, we use the ozone coupled ECCC GDPS to assess the impact of ozone radiative forcing on the accuracy of ozone and weather forecasts during major springtime ozone depletion events in both polar regions in 2020. The NWP model employs a linearized gas-phase photochem-

ical module along with a simplified parameterization scheme to represent the ozone loss associated with the important heterogeneous reactions occurring during polar ozone depletion events.

The study shows that the predictability of TOC is relatively high during ozone depletion events, exceeding 10 days in both polar regions. In the SH, results indicate that ozone mean biases against GDPS analyses decreased by about 75% in August and September throughout the lower stratosphere with the use of the heterogeneous chemistry parameterization scheme. Implementing this process in the model has also contributed to improving TOC predictability by about 8 hours during the same period, indicating a significant reduction in ozone modeling errors. In the NH, the parameterization scheme has helped reduce TOC biases by about 40% in February and March at all lead times, including a few percent reduction in the standard deviation.

The use of ozone as a radiatively active constituent had a significant impact on the quality of weather forecasts throughout the lower stratosphere in both polar regions. In the SH, the use of an ozone coupled NWP model has contributed to improving the temperature and zonal wind distribution in the forecasts at all lead times. The study shows that the mean temperature forecast during the SH springtime period has decreased by about 0.5 degrees at 5-day lead times, which has also contributed to increasing the zonal wind field by about 0.5 m/s through thermal wind balance, in better agreement with GDPS analyses. The inclusion of ozone radiative coupling has also contributed to increasing temperature predictability by about 12 hours at 70 hPa, demonstrating the model's capability to resolve the radiative and photochemical interactions between temperature and ozone at those timescales. Over the Arctic the radiative impact of ozone is significantly weaker due to the large dynamical variability of the region. During the 2020 winter period, the impact of ozone radiative coupling on weather forecasts is particularly significant in March, when ozone depletion processes and ozone heating become significant. In such conditions, the use of an ozone coupled forecasting system reduces the temperature bias that develops at short lead times with the use of a prescribed ozone climatology. The results also show that most of the improvement in temperature and wind forecasts within 10-day lead times in both hemispheres is associated with the quality of ozone analyses, which serve as initial conditions, and the representation of ozone transport processes in the NWP model.

The study highlights the importance of improving the representation of ozone heating within NWP forecasting systems. It shows that the radiative impact of ozone over polar regions develops

rapidly and can significantly improve the quality of weather forecasts. The study demonstrates that the coupling mechanisms between ozone and temperature can be represented at medium-range timescales with the use of ozone assimilation and a simplified modeling approach.

The results also indicate that the radiative impact of ozone on weather increases steadily over time and will likely affect weather predictability at monthly and seasonal timescales. At those timescales, the influence of the ozone initial conditions will decrease, and the quality of the ozone forecasts will be mainly determined by modeling errors. In this context, the use of ozone coupled systems for monthly and seasonal forecasting will likely necessitate the development of more comprehensive modeling approaches (e.g. Monge-Sanz et al. (2011)) that will further extend ozone predictability throughout the UTLS region.

APPENDIX

A1. On the representation of ozone over the Arctic

The ozone hole area, defined as the region encircled by the TOC 220 DU contour, is typically used for characterizing the extent of the ozone depletion process. The size of the area varies significantly and reached a maximum of slightly over 1 million km^2 in mid-March (Dameris et al. 2021). The GDPS analysis on March 28th (Fig.A1 - left panel) shows that the ozone hole is located north of Greenland, in good agreement with OMI measurements (Fig.A1 - right panel), even though the TOC values appear slightly overestimated by the GDPS. Fig.A2 shows the GDPS ozone profile for the same day at Ny-Alesund, which is compared against an in-situ ozonesonde observation. Results show that the signature of the ozone depletion around 70 hPa is well represented in the analyses.
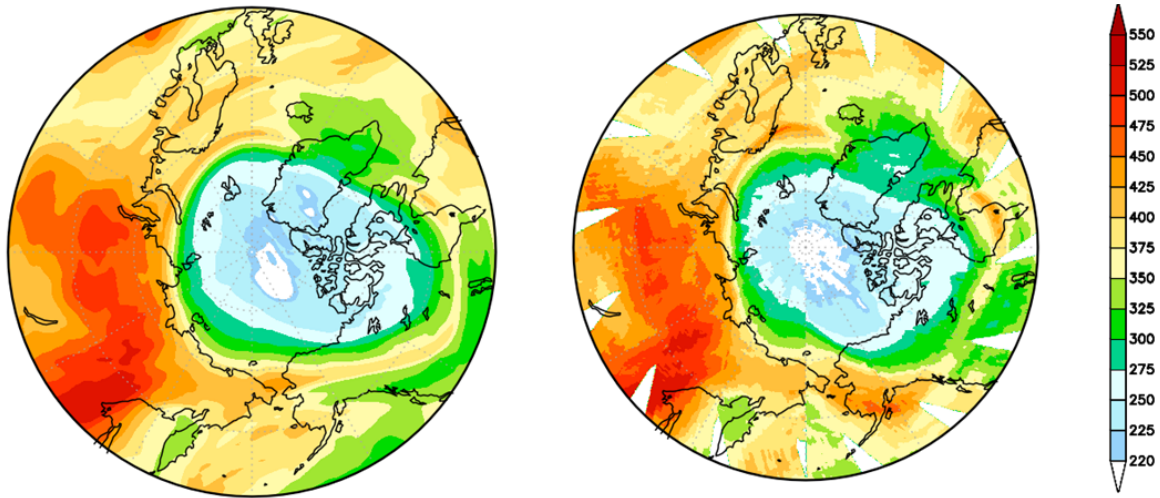
Fig.A1. TOC (DU) over the Arctic on March 28th 2020 from (left) GDPS analyses and (right) OMI .
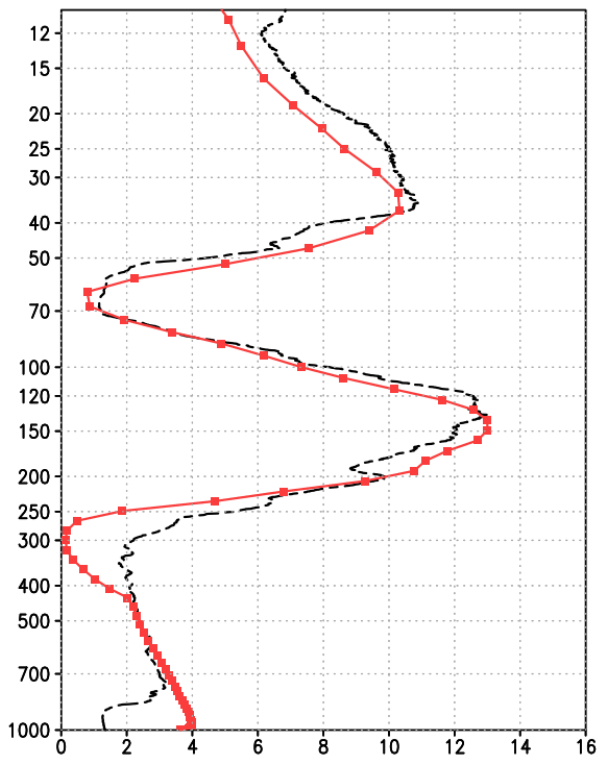

Fig.A2. Ozone profiles at Ny Alesund (78.9N, 11.9E) on March 28th 2020 from the GDPS (red) and the ozonesonde (black).

References

Andrews, D. G., J. R. Holton, and C. B. Leovy, 1987: Middle atmospheric dynamics. *Academic Press*, 489 pp.

Bai, K., N. Chang, H. Yu, and W. Gao, 2016: Statistical bias correction for creating coherent total ozone record from omi and omps observations. *Remote Sens. Environ.*, **182**, 150–168, https://doi.org/10.1016/j.rse.2016.05.007.

Baldwin, M., and T. Dunkerton, 1999: Propagation of the arctic oscillation from the stratosphere to the troposphere. *J. Geophys. Res.*, **104**, 30 937–30 946, https://doi.org/10.1029/1999JD900445.

Baldwin, M., and Coauthors, 2021: Sudden stratospheric warmings. *Rev. Geophys.*, **59**, https://doi.org/10.1029/2020RG000708.

Bharthia, P. K., and C. Wellemeyer, 2002: Toms-v8 total o3 algorithm. *OMI Algorithm Theoretical Basis Document*, **2**, 15–31.

Buehner, M., and Coauthors, 2015: Implementation of deterministic weather forecast systems based on ensemble-variational data assimilation at environment canada, part 1: The global system. *Monthly Weather Review*, **143**, 2532–2559, https://doi.org/10.1175/MWR-D-14-00354.1.

Cariolle, D., and H. Teyssèdre, 2007: A revised linear ozone photochemistry parameterization for use in transport and general circulation models: multi-annual simulations. *Atmos. Chem. Phys.*, **7**, 2183–2196, https://doi.org/10.5194/acp-7-2183-2007.

Charney, J., and P. Drazin, 1961: Propagation of planetary-scale disturbances from the lower to the upper atmosphere. *J. Geophys. Res.*, **66**, https://doi.org/10.1029/JZ066i001p00083.

Charron, M., and Coauthors, 2012: The stratospheric extension of the Canadian global deterministic medium-range weather forecasting system and its impact on tropospheric forecasts. *Mon. Wea. Rev.*, **140**, 1924–1944, https://doi.org/10.1175/MWR-D-11-00097.1.

Côté, J., S. Gravel, A. Méthot, A. Patoine, M. Roch, and A. Staniforth, 1998: The operational CMC-MRB Global Environmental Multiscale (GEM) model. Part I: Design considerations and formulation. *Mon. Wea. Rev.*, **126**, 1373–1395, https://doi.org/10.1175/1520-0493(1998)126⟨1373:TOCMGE⟩2.0.CO;2.

Crook, J., N. Gillet, and S. Keeley, 2008: Sensitivity of southern hemisphere climate to zonal asymmetry in ozone. *Geophys. Res. Lett.*, **35**, https://doi.org/10.1029/2007GL032698.

Dameris, M., D. Loyola, M. Nutzel, M. Coldewey-Egbers, C. Lerot, F. Romahn, and M. van Roozendael, 2021: Record low ozone values over the arctic in boreal spring 2020. *Atmos. Chem. Phys.*, **21**, 617–633, https://doi.org/10.5194/acp-21-617-2021.

de Grandpré, J., R. Ménard, Y. J. Rochon, C. Charette, S. Chabrillat, and A. Robichaud, 2009: Radiative impact of ozone on temperature predictability in a coupled chemistry-dynamics data assimilation system. *Mon. Wea. Rev.*, **137**, 679–692, https://doi.org/10.1175/2008MWR2572.1.

de Grandpré, J., M. Tanguay, A. Qaddouri, M. Zerroukat, and C. A. McLinden, 2016: Semi-lagrangian advection of stratospheric ozone on a yin–yang grid system. *Mon. Wea. Rev.*, **144**, 1035–1050, https://doi.org/10.1175/MWR-D-15-0142.1.

Desroziers, G., L. Berre, B. Chapnik, and P. Poli, 2005: Diagnosis of observation, background, and analysis-error statistics in observation space. *Q. J. R. Meteorol. Soc.*, **131**, 3385–3396, https://doi.org/10.1256/qj.05.108.

Efron, B., and T. Tibshirani, Eds., 1994: *An Introduction to the Bootstrap*. Chapman and Hall/CRC, 456 pp., https://doi.org/10.1201/9780429246593.

Eskes, H., P. van Velthoven, and H. Kelder, 2002: Global ozone forecasting based on ers-2 gome observations. *Atmos. Chem. Phys.*, **2**, 271–278, https://doi.org/10.5194/acp-2-271-2002.

Flemming, J., and Coauthors, 2011: Forecasts and assimilation experiments of the antarctic ozone hole 2008. *Atmos. Chem. Phys.*, **11**, 1961–1977, https://doi.org/10.5194/acp-11-1961-2011.

Flynn, L., C. Seftor, J. Larsen, and P. Xu, 2006: The ozone mapping and profiler suite in :. *Earth Science Satellite Remote Sensing*, J. Qu, W. Gao, M. Kafatos, R. Murphy, and V. Salomonson, Eds., Springer, Berlin, Heidelberg, https://doi.org/10.1007/978-3-540-37293-6_15.

Flynn, L., Z. Zhang, V. Mikles, B. Das, J. Niu, C. Beck, and E. Beach, 2017: Algorithm theoretical basis document for noaa nde omps version 8 ozone profile (v8pro) environmental data record (edr) version 1.0. *Satellite Products and Services Review Board, NOAA*.

Fortuin, J. P., and H. Kelder, 1998: An ozone climatology based on ozonesonde and satellite measurements. *J. Geophys. Res.*, **103**, 31 709–31 734, https://doi.org/10.1029/1998JD200008.

Garane, K., and Coauthors, 2019: Tropomi/s5p total ozone column data: global ground based validation and consistency with other satellite missions. *Atmos. Meas. Tech.*, **12**, 5263–5287, https://doi.org/10.5194/amt-12-5263-2019.

Geer, A., 2016: Significance of changes in medium-range forecast scores. *Tellus*, **68A**, 305–320, https://doi.org/10.3402/tellusa.v68.30229.

Geer, A. J., W. A. Lahoz, D. R. Jackson, D. Cariolle, and J. P. McCormack, 2007: Evaluation of linear ozone photochemistry parametrizations in a stratosphere-troposphere data assimilation system. *Atmos. Chem. Phys.*, **7**, 939–959, https://doi.org/10.5194/acp-7-939-2007.

Geer, A. J., and Coauthors, 2006: The ASSET intercomparison of ozone analyses: method and first results. *Atmos. Chem. Phys.*, **6**, 5445–5474, https://doi.org/10.5194/acp-6-5445-2006.

Gillet, N., J. Scinocca, D. Plummer, and M. Reader, 2009: Sensitivity of climate to dynamically-consistent zonal asymmetries in ozone. *Geophys. Res. Lett.*, **36**, L10 809, https://doi.org/10.1029/2009GL037246.

Girard, C., and Coauthors, 2014: Staggered Vertical Discretization of the Canadian Environmental Multiscale (GEM) model using a coordinate of the log-hydrostatic-pressure type. *Mon. Wea. Rev.*, **142**, 1183–1196, https://doi.org/10.1175/MWR-D-13-00255.1.

Haase, S., and K. Matthes, 2019: The importance of interactive chemistry for stratospheric-tropospheric coupling. *Atmos. Chem. Phys.*, **19**, 3417–3432, https://doi.org/10.5194/acp-19-3417-2019.

Hand, E., 2016: Record ozone hole may open over arctic in the spring. *Science*, **351**, 650, https://doi.org/10.1126/science.351.6274.650.

Haynes, P., M. McIntyre, T. Shepherd, C. Marks, and K. Shine, 1991: On the "downward control" of extratropical diabatic circulations by eddy-induced mean zonal forces. *J. Atmos. Sci.*, **48**, 651–678, https://doi.org/10.1175/1520-0469(1991)048⟨0651:OTCOED⟩2.0.CO;2.

Hersbach, H., and Coauthors, 2020: The ERA5 global reanalysis. *Quart. J. Roy. Meteor. Soc.*, **146(730)**, https://doi.org/10.1002/qj.3803.

Hines, C. O., 1997: Doppler-spread parameterization of gravity-wave momentum deposition in the middle atmosphere Part1: Basic formulation. *J. Atmos. Sol.-Terr. Phys.*, **59**, 371–386.

Holton, J., P. Haynes, M. McIntyre, A. Douglass, R. Rood, and L. Pfister, 1995: Stratosphere-troposphere exchange. *Rev. Geophys.*, **33**, 403–439.

Hsu, J., and M. Prather, 2009: Stratospheric variability and tropospheric ozone. *J. Geophys. Res.*, **114**, https://doi.org/10.1029/2008JD010942.

Husain, S. Z., and C. Girard, 2017: Impact of consistent semi-lagrangian trajectory calculations on numerical weather prediction performance. *Mon. Wea. Rev.*, **145**, 4127–4150, https://doi.org/10.1175/MWR-D-17-0138.1.

Inness, A., S. Chabrillat, J. Flemming, V. Huijnen, B. Langenrock, J. Nicolas, I. Polichtchouk, and M. Razinger, 2020: Exceptionally low arctic stratospheric ozone in spring 2020 as seen in the cams reanalysis. *J. Geophys. Res.*, **125**, https://doi.org/10.1029/2020JD033563.

Inness, A., and Coauthors, 2019: The cams reanalysis of atmospheric composition. *Atmos. Chem. Phys.*, **19**, 3515–3556, https://doi.org/10.5194/acp-19-3515-2019.

Lawrence, Z., and G. Manney, 2020: Does the arctic stratospheric polar vortex exhibit signs of preconditioning prior to sudden stratospheric warmings? *J. Atmos. Sci.*, **77**, 611–632, https://doi.org/10.1175/JAS-D-19-0168.1.

Lawrence, Z., J. Perlwitz, A. Butler, G. Manney, P. Newman, S. Lee, and E. Nash, 2020: The remarkably strong arctic stratospheric polar vortex of winter 2020: Links to record-breaking arctic oscillation and ozone loss. *J. Geophys. Res.*, **125**, https://doi.org/10.1029/2020JD033271.

Li, J., and H. W. Barker, 2005: A radiation algorithm with correlated k-distribution. Part I: local thermal equilibrium. *J. Atmos. Sci.*, **62**, 286–309, https://doi.org/10.1175/JAS-3396.1.

Lin, P., D. Paynter, L. Polvani, G. Correa, Y. Ming, and V. Ramaswamy, 2017: Dependance of model-simulated response to ozone depletion on stratospheric polar vortex climatology. *Geophys. Res. Lett.*, **44**, 6391–6398, https://doi.org/10.1029/2020GL073862.

Manney, G., and Coauthors, 2020: Record-low arctic stratospheric ozone in 2020: Mls observations of chemical processes and comparisons with previous extreme winters. *Geophys. Res. Lett.*, **47**, https://doi.org/10.1029/2020GL089063.

McCormack, J., S. Eckermann, D. Siskind, and T. McGee, 2006: Chem2d-opp: A new linearized gas-phase ozone photochemistry parameterization for high-altitude nwp and climate models. *Atmos. Chem. Phys.*, **6**, 4943–4972, https://doi.org/10.5194/acp-6-4943-2006.

McLinden, C. A., S. C. Olsen, B. Hannegan, O. Wild, and M. J. Prather, 2000: Stratospheric ozone in 3-D models: A simple chemistry and the cross-tropopause flux. *J. Geophys. Res.*, **105**, 14 653–14 665, https://doi.org/10.1029/2000JD900124.

McPeters, R., P. Bhartia, D. Haffner, G. Labow, and L. Flynn, 2013: The version 8.6 sbuv ozone data record: An overview. *J. Geophys. Res.*, **118**, 1–8, https://doi.org/10.1002/jgrd.50597.

McTaggart-Cowan, R., and Coauthors, 2019: Modernization of atmospheric physics parameterization in canadian nwp. *Journal of advances in Modelling Earth Systems*, **11**, 3593–3635, https://doi.org/10.1029/2019MS001781.

Ménard, R., and Coauthors, 2019: Coupled stratospheric chemistry-meteorology data assimilation. part 1: Physical background and coupled modeling aspects. *Atmosphere*, **11**, https://doi.org/10.3390/atmos11020150.

Monge-Sanz, B., M. Chipperfield, D. Cariolle, and W. Feng, 2011: Results from a new linear o^3 schem with embedded heterogeneous chemistry compared with the parent full-chemistry 3-d ctm. *Atmos. Chem. Phys.*, **11**, 1227–1242, https://doi.org/10.5194/acp-11-1227-2011.

Monge-Sanz, B., and Coauthors, 2022: A stratospheric prognostic ozone for seamless earth system models: performance, impacts and future. *Atmos. Chem. Phys.*, **22**, 4277–4302, https://doi.org/10.5194/acp-22-4277-2022.

Oh, J., S. Son, J. Choi, E. Lim, C. Garfinkel, H. Hendon, Y. Kim, and H. Kang, 2022: Impact of stratospheric ozone on the subseasonal prediction in the southern hemisphere spring. *Progress in Earth and Planetary Science*, **9(25)**, 150–168, https://doi.org/10.1186/s40645-022-00485-4.

Qaddouri, A., and V. Lee, 2011: The Canadian Global Environmental Multiscale model on the Yin-Yang grid system. *Q. J. Roy. Meteor. Soc.*, **137**, 1913–1926, https://doi.org/10.1002/qj.873.

Rochon, Y., M. Sitwell, and Y. Cho, 2019: A study on harmonizing total ozone assimilation with multiple sensors. *Atmos. Chem. Phys.*, **19**, 9431–9451, https://doi.org/10.5194/acp-19-9431-2019.

Scaife, A., and Coauthors, 2014: Predictability of the quasi-biennial oscillation and its northern winter teleconnection on seasonal to decadal timescales. *Geophys. Res. Lett.*, **41**, 1752–1758, https://doi.org/10.1002/2013GL059160.

Scaife, A., and Coauthors, 2022: Long-range prediction and the stratosphere. *Atmos. Chem. Phys.*, **22**, 2601–2623, https://doi.org/10.5194/acp-22-2601-2022.

Sekiyama, T., and K. Shibata, 2005: Predictability of total ozone using a global three-dimensional chemical transport model coupled with the mri/jma98 gcm. *Mon. Wea. Rev.*, **133**, 2262–2274, https://doi.org/10.1175/MWR2976.1.

Solomon, S., 1999: Stratospheric ozone depletion: a review of concepts and history. *Rev. of Geophys.*, **37**, 275–316, https://doi.org/10.1029/1999RG900008.

Stajner, I., K. Wargan, L. Chang, H. Hayashi, S. Pawson, and H. Nakajima, 2006: Assimilation of ozone profiles from the improved limb atmospheric spectrometer-ii: Study of antarctic ozone. *J. Geophys. Res.*, **111**, D11S14, https://doi.org/10.1025/2005JD006448.

Wang, W., J. Hong, M. Shangguan, H. Wang, W. Jiang, and S. Zhao, 2022: Zonally asymmetric influences of the quasi-biennial oscillation on stratospheric ozone. *Atmos. Chem. Phys.*, **22(20)**, 13 695–13 711, https://doi.org/10.5194/acp-22-13695-2022.

Wargan, K., B. Weir, G. Manney, S. Cohn, K. Knowland, P. Wales, and N. Livesey, 2023: M2-scream: A stratospheric composition reanalys is of aura mls data with merra-2 transport. *Earth and Space Science*, **10(2)**, https://doi.org/10.1029/2022EA002632.

Witze, A., 2020: Rare ozone hole opens over the arctic - and it's big. *nature*, **580**, 18–19, https://doi.org/10.1038/d41586-020-00904-w.

WMO, 2018: Scientific Assessment of Ozone Depletion: 2018. Global Ozone Research and Monitoring Project-Report no. 55, World Meteorological Organization, Geneva, Switzerland, 588 pp.